



## Stress measurement at the interface between a Si substrate and diamond-like carbon/Cr/W films by the electronic backscatter diffraction method

Liqi Zhou<sup>1,2</sup>, Guofu Xu<sup>1</sup>, Xu Li<sup>2</sup>, Xinwei Wang<sup>3</sup>, Lingling Ren<sup>2</sup>, Aiyong Wang<sup>4\*</sup>, and Xingfu Tao<sup>2\*</sup>

<sup>1</sup>School of Materials Science and Engineering, Central South University, Changsha 410083, China

<sup>2</sup>Division of Nano Metrology and Materials Measurement, National Institute of Metrology, Beijing 100013, China

<sup>3</sup>Research Institute of Surface Engineering, Taiyuan University of Technology, Taiyuan 030000, China

<sup>4</sup>Key Laboratory of Marine Materials and Related Technology, Zhejiang Key Laboratory of Marine Materials and Protection Technology, Ningbo Institute of Material Technology and Engineering, Chinese Academy of Sciences, Ningbo 315201, China

\*E-mail: aywang@nimte.ac.cn; taoxf@nim.ac.cn

Received December 3, 2015; accepted December 28, 2015; published online January 20, 2016

Stress distribution characteristics at the interface between diamond-like carbon (DLC)/Cr/W films and a Si substrate were studied by an electronic backscatter diffraction (EBSD) system and transmission electron microscopy. Positive and negative stresses were distributed within the largest width of the Si/DLC interface, whereas the stress bands of homogeneous stress layers were observed at the interface between the Si substrate and the Cr layer. The stress bands of the Si/W interface were found to have the smallest width. The distinct characteristics of stress distribution at these interfaces are produced by the difference in the mass, energy, and diameter of the deposition ions/atoms as well as the different mechanisms of film growth. © 2016 The Japan Society of Applied Physics

**D**iamond-like carbon (DLC) and metallic thin films are important components of fast developing micro-devices and microsystems. Residual stress has an important effect on the microstructure and properties of such films. Researchers have found that through the control of residual stress, the mechanical properties of thin film/substrate systems, especially cohesion, can be markedly improved. Therefore, accurate and reliable residual stress evaluation at the micro- and even sub-microscale is critical for improving the reliability and production of thin-film-based mechanical/electronic devices.

The curvature method is most commonly used in studying film/substrate systems. It offers a convenient way of monitoring small variations in substrate curvature from which average stress values in both crystalline and amorphous films can be obtained using relatively simple-to-use, commercially available experimental systems.<sup>1,2</sup> This method is commonly used for macro-scale systems. Micro-Raman spectroscopy has been used for analyzing stress in films based on the spectroscopic shift of their Raman spectrum induced by a local distortion<sup>3,4</sup> but is restricted by the difficulty in determining the detailed components of the strain tensor.

X-ray diffraction is perhaps the most well developed method for residual stress measurement.<sup>5,6</sup> It relies on measurements of elastic strains from changes in the lattice spacing caused by stress. Such elastic strains are converted to average stress values from known elastic constants (ECs) of the stressed material. The use of conventional X-ray diffraction is restricted to crystalline thin films and its spatial resolution is, at best, about 100 μm.<sup>7</sup> A more advanced methodology using synchrotron sources can measure the elastic strain of amorphous material and lead to considerable improvement in spatial resolution,<sup>8</sup> however, complex procedures and lack of equipment availability prevent its widespread application in residual stress measurement.

The various methods for residual stress evaluation described above, while benefiting from their nondestructive nature, have a number of limitations. Moreover, only volume-averaged stress values can be measured by these techniques but little information about stress distribution at the sub-micron scale can be extracted, that is closely associated

with the macro-mechanical properties of thin film-based devices.<sup>9</sup> Electron backscatter diffraction (EBSD) that determines elastic strains and lattice rotations based on cross correlation image analysis of small shifts in the EBSD patterns provides another powerful technique to analyze residual stress at the sub-micrometer scale.<sup>10</sup> The utilization of this technique in the characterization of strain/stress has attracted attention because of its unique advantages, such as ultrahigh spatial resolution, easy sample preparation, and high-speed data acquisition. Moreover, each tensor component can be quantitatively mapped by the method. In the last decade, the accuracy and sensitivity of strain and rotation measurement using EBSD has been widely studied.<sup>11,12</sup> There are, however, limited reports on the application of this method in stress/strain measurement of the film/substrate interface.<sup>13,14</sup>

In our previous studies, the strain distribution around nanoindentations on single-crystal silicon was two-dimensionally mapped by using EBSD and CrossCourt software with high strain resolution.<sup>15,16</sup> In this work, we focus on the measurement of stress at the interface of Si/DLC, Si/Cr, and Si/W systems by employing EBSD and CrossCourt analysis, which has not been widely studied. Furthermore, the distinct characteristics of stress distribution in these systems are discussed based on the mechanism of stress evolution combined with high-resolution electron microscopy (HREM) and electron spectroscopic imaging (ESI) observations.

The test films were prepared by a unique hybrid ion beam deposition system that consists of a DC magnetron sputtering source Cr/W (99.99%) target and a linear source. Cr and W films were deposited on single-crystal Si wafers with Ar<sub>2</sub> gas flux of 55 sccm, voltage of 400 V, current of 3 A, biased voltage of -100 V, and deposition time of 20 min. The DLC film was prepared by the hybrid ion beam deposition system with C<sub>2</sub>H<sub>2</sub> gas flux of 40 sccm, voltage of 1200 V, current of 0.2 A, and biased voltage of -100 V. The cross-section EBSD and TEM samples were prepared by using the Leica EM TXP mechanical milling system and Leica RES 101 ion milling system. For EBSD testing, the cross-section of the specimens was slowly single-side polished to 200-μm-thick and then ion-milled for 30 min. For TEM testing, the specimens were double-side polished to 20-μm-thick, then

double-side ion-milled on a molybdenum ring holder to gain appropriate thinned areas for HREM.

Full resolution ( $1344 \times 1024$  pixels) diffraction patterns of the film/substrate interface were captured from the Si side near the interface with a Nordlys Nano EBSD detector embedded in a Zeiss Ultra 55 scanning electron microscope (SEM). The microscope worked at an acceleration voltage of 25 kV, with a stage tilt of  $70^\circ$ . The working distance and scanning step were set to 12 mm and 20 nm, respectively and pattern acquisition of every  $84 \times 48$  pixel area lasted for approximately 30 min. All EBSD-Kikuchi patterns were processed by the commercial software, CrossCourt 3 (BLG production), that had a disorientation sensitivity of  $\pm 0.006^\circ$  and a strain sensitivity of  $\pm 10^{-4}$  for residual strain/stress calculation.<sup>10)</sup>

The analysis method relies on the fact that elastic strain and lattice rotation cause small shifts in features, such as zone axis, within the EBSD-Kikuchi patterns.<sup>17,18)</sup> By comparing a testing pattern with the reference pattern of a strain-free point, small shifts are detected at sub-pixel resolution through cross-correlation-based pattern shift analysis. The small shift is then geometrically converted to the displacement gradient tensor (**A**) that is defined as

$$\mathbf{A} = \begin{pmatrix} \frac{\partial \mu_1}{\partial x_1} & \frac{\partial \mu_1}{\partial x_2} & \frac{\partial \mu_1}{\partial x_3} \\ \frac{\partial \mu_2}{\partial x_1} & \frac{\partial \mu_2}{\partial x_2} & \frac{\partial \mu_2}{\partial x_3} \\ \frac{\partial \mu_3}{\partial x_1} & \frac{\partial \mu_3}{\partial x_2} & \frac{\partial \mu_3}{\partial x_3} \end{pmatrix}, \quad (1)$$

where  $\mu = (\mu_1, \mu_2, \mu_3)$  is the displacement at position  $x = (x_1, x_2, x_3)$  within the sample. According to the theory of elasticity, strain tensor  $e_{ij}$  and rotation tensor  $w_{ij}$  are deduced from the symmetric and antisymmetric part of **A**, respectively, using the following equations:

$$e_{ij} = \frac{1}{2} \left( \frac{\partial \mu_i}{\partial x_j} + \frac{\partial \mu_j}{\partial x_i} \right) \quad (2)$$

$$w_{ij} = \frac{1}{2} \left( \frac{\partial \mu_i}{\partial x_j} - \frac{\partial \mu_j}{\partial x_i} \right) \quad (3)$$

The point at which the pattern possessed the highest image quality (IQ) value was selected as the reference in the single-crystal Si substrate far from the film/substrate interface that is strain-free (or the least strained). For cross correlation, five different regions of interest (ROIs) of all the patterns were compared against the same regions in the reference pattern, and the appropriate stored set of ECs of single-crystal Si was chosen. Therefore, the strain/stress of entire points in the EBSD testing area was calculated.

HREM and ESI observations of the film-substrate interfaces were performed on a Zeiss Libra 200 field-emission TEM operating at 200 kV.

Stresses at the interfaces between the Si substrate and DLC/Cr/W films are quantitatively mapped and displayed in the Figs. 1–3, in which the colored region refers to the Si substrate, and the white area at the right side refers to the film. Moreover, the black spot in the Si substrate region refers to the reference, while the other region of deeper color refers to the interface stress state on the Si side. In other words, the deeper colored region is the interfacial stress bands occurring in the Si substrate.

Figure 1 presents six stress components of the Si substrate near the Si/DLC interface and clear SEM image of the interface. It can be seen that positive and negative stress values are distributed in stress bands with widths of about 400 nm. The peak value of positive and negative stresses reaches about 30 GPa except for the stress value of the  $\sigma_{zz}$  component, which is around 0 due to stress relaxation.

As shown in Fig. 2, stress components of the Si substrate near the Si/Cr interface present bands with homogeneous stress (either positive or negative) layers. Three positive stress layers that have approximate widths of 200 nm are formed near the interface for the  $\sigma_{xx}$ ,  $\sigma_{yy}$ , and  $\sigma_{xy}$  components and maximum stress values of the  $\sigma_{xx}$ ,  $\sigma_{yy}$ , and  $\sigma_{xy}$  components are 60, 120, and 30 GPa, respectively. Moreover, three narrow negative stress layers are found between the Si and the positive stress layers, with approximate width and maximum stress value of 20 nm and  $-20$  GPa, respectively. On the other hand, the stress distribution for the  $\sigma_{xz}$  and  $\sigma_{yz}$  components has similar characteristics to that of the  $\sigma_{xx}$ ,  $\sigma_{yy}$ , and  $\sigma_{xy}$  components, except with opposite stress directions and smaller stress magnitudes. The stress value of the  $\sigma_{zz}$  component is still around 0, in line with expectations. It is noted that the stress bands are distorted owing to the drift of the sample stage; however, such a small drift (about 100 nm estimated from the scale bar) has little effect on the stress calculation.

Figure 3 reveals that the stress bands of the Si/W interface are extremely narrow compared with that of the Si/DLC and Si/Cr interfaces. The positive and negative stress values have a mixed distribution, which is similar to that of the Si/DLC interface. The peak values of positive and negative stresses reach about 10 and  $-20$  GPa, respectively, while the stress value of the  $\sigma_{zz}$  component is still around 0. It is noted that the inclined right edges are due to the drift of the sample stage during the pattern acquisition, the same as for the Si/Cr interface with the distorted stress bands in Fig. 2. Such a drift has little effect on the stress distribution calculation.

The high-resolution microstructure and elemental mapping of the interfaces between the Si substrate and DLC/Cr/W films are displayed in Fig. 4. The high-resolution microstructure and the element mapping of Si at these interfaces show that there is a well-defined intermediate layer at each of the three interfaces. However, the widths of the intermediate layer of the three interfaces are different, the largest width being for the Si/DLC interface while the layer at the Si/W interface is very small, which is consistent with the EBSD observations above. The selected area diffraction analysis reveals that the DLC film is amorphous, and the Cr and W films are polycrystalline.

Fundamentally, the distinct characteristics of stress distribution at the three interfaces are because of the difference in the mass, energy, and diameter of the deposition ions/atoms as well as the different mechanisms of film growth. The stress produced in substrate/film systems consists of thermal stress, interfacial stress, and growth stress. In this work, the thermal stress is ignored due to the small temperature change during the deposition process.<sup>19)</sup> At the initial stage of the deposition process, high-energy ions/atoms deposit on and penetrate the Si substrate, which leads to the lattice distortion of Si and the following interfacial stress. The atomic collision mechanism is given by<sup>20)</sup>

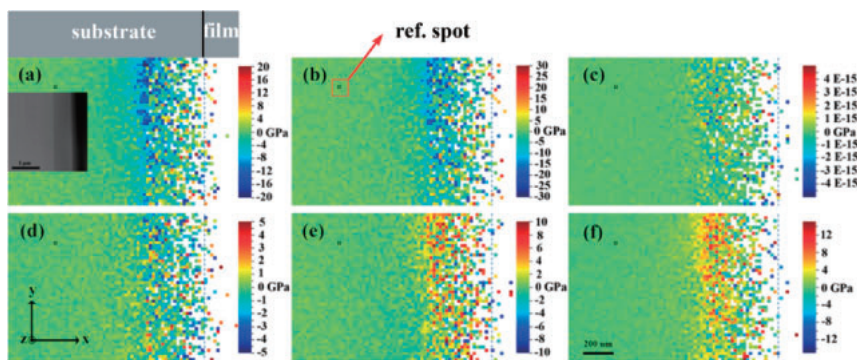


**Fig. 1.** Residual stress distribution of Si substrate at Si/DLC interface: (a)  $\sigma_{xx}$ ; (b)  $\sigma_{yy}$ ; (c)  $\sigma_{zz}$ ; (d)  $\sigma_{xy}$ ; (e)  $\sigma_{xz}$ ; (f)  $\sigma_{yz}$ . The EBSD pattern of the black spot is the reference.

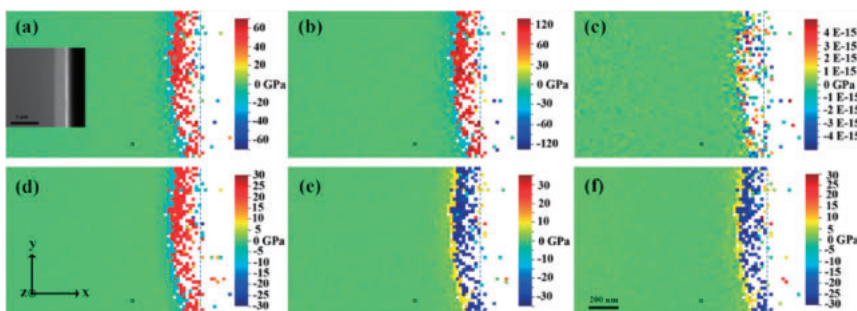


**Fig. 2.** Residual stress distribution of Si substrate at Si/Cr interface: (a)  $\sigma_{xx}$ ; (b)  $\sigma_{yy}$ ; (c)  $\sigma_{zz}$ ; (d)  $\sigma_{xy}$ ; (e)  $\sigma_{xz}$ ; (f)  $\sigma_{yz}$ . The EBSD pattern of the black spot is the reference.

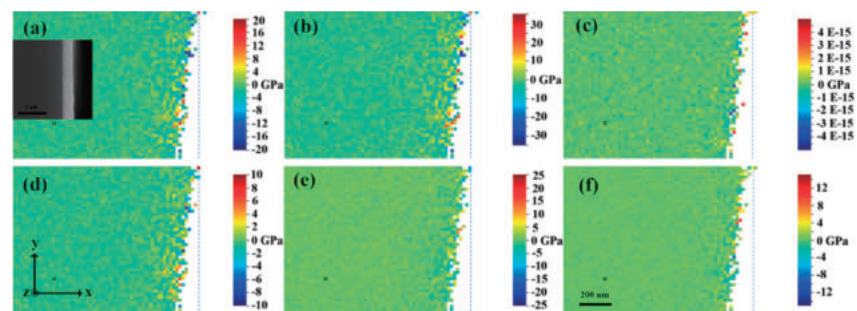


**Fig. 3.** Residual stress distribution of Si substrate at Si/W interface: (a)  $\sigma_{xx}$ ; (b)  $\sigma_{yy}$ ; (c)  $\sigma_{zz}$ ; (d)  $\sigma_{xy}$ ; (e)  $\sigma_{xz}$ ; (f)  $\sigma_{yz}$ . The EBSD pattern of the black spot is the reference.

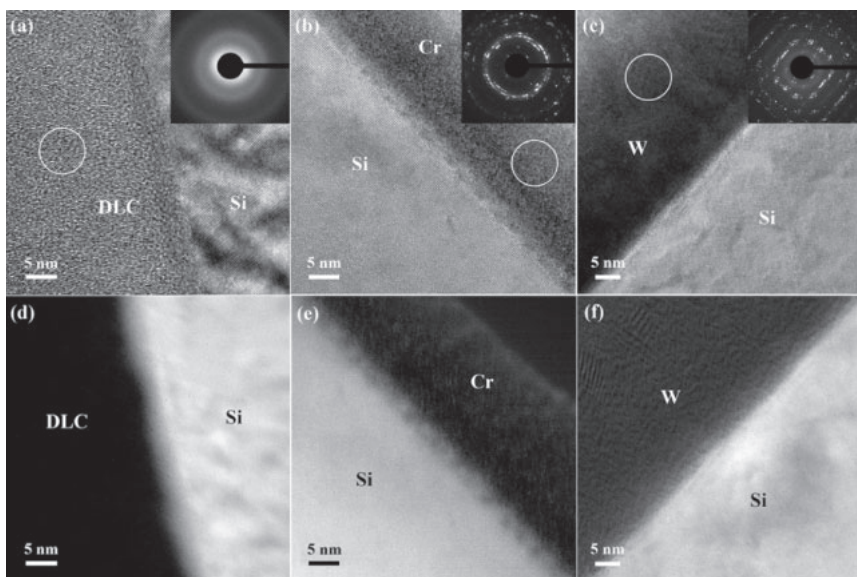


**Fig. 4.** TEM image and element distribution of Si-DLC/Cr/W interfaces. (a)–(c) HREM images of (a) Si–DLC, (b) Si–Cr, and (c) Si–W interfaces. (d)–(f) ESI images of Si mapping at the (d) Si–DLC, (e) Si–Cr, and (f) Si–W interfaces (white zones).

$$E_1 = \frac{4M_0M_1}{(M_0 + M_1)^2} E_0 \cos^2 \theta, \quad (4)$$

where  $M_0$  and  $E_0$  are, respectively, the mass and energy of incident ions that bombard the metal targets,  $M_1$  and  $E_1$  are the mass and energy of the sputtered metal atoms, respectively, and  $\theta$  is the recoil angle. A simple analysis of Eq. (4) shows that given the same  $M_0$ ,  $E_0$ , and  $\theta$ ,  $E_1$  decreases as  $M_1$  increases. As the relative atomic mass of the Cr and W atom is 51.996 and 183.85, respectively, the obtained energy of the Cr atom is larger than that of the W atom before they deposit on the Si substrate, which means that the Cr atoms gain a wider impact area on the substrate. Meanwhile, the smaller diameter of the Cr atom compared to the W atom may lead to wider stress layers in the Si/Cr system compared to the Si/W system. It is assumed that the C ions obtain the largest energy before they deposit on the Si substrate, because of the higher sputtering voltage of the C ion (1200 V) during the ion beam deposition compared to that of the Cr and W atoms. Moreover, as the C ion has a smaller diameter than the Cr and W atoms, it may penetrate the Si substrate deeply and result in the wider stress bands seen in the Si/DLC system.

The DLC film grows into an amorphous structure via the subplantation mechanism.<sup>21,22</sup> Incident C ions penetrate the Si subsurface and form  $sp^3$  bonds that lead to the formation of thermal spike regions, elastic expansion, and compressive stress. The region mixed with C species and Si atoms is continuously bombarded by C ions until a pure carbon layer is formed. Meanwhile, a metastable  $sp^3$  state of C species is produced by the energy transmission of the thermal spike region and ion bombardment that results in the detrapping of C species. The  $sp^3$  fraction that is inherently related to the film stress is thus determined by the equilibrium between the densification and detrapping processes. The evolution of growth stress in the C film leads to the variation of interfacial stress of the Si/DLC system and the final steady-state stress is obtained at the interruption of film growth.

On the other hand, Cr and W films grow into a polycrystalline structure via the Volmer–Weber mechanism: with processes of island nucleation, growth, and coalescence,<sup>23</sup> in which either compressive or tensile stress will be produced in the film. The initial compressive stress is due to the formation of isolated islands and the tensile stress is produced due to the growth and contact of the isolated islands,<sup>24,25</sup> and increased to a maximum value when the film is completely covered the substrate. The tensile stress relaxes and eventually becomes compressive with continued deposition.<sup>26,27</sup> Therefore, the steady-state stress depends on the film structure at which growth is interrupted, which will in turn determine the stress distribution of the interface.

In conclusion, the stress distribution characteristics at the interfaces between a Si substrate and DLC/Cr/W films were studied by SEM-based EBSD and TEM. It was shown that

the stress bands of the DLC/substrate are mixed with positive and negative stress values and have largest widths of about 400 nm. Stress bands of homogeneous layers with widths of about 200 and 20 nm are generated at the Si/Cr interface and the stress bands of the Si/W interface have positive and negative stresses with smaller widths. The cause of the distinct characteristics of stress distribution at these interfaces is complex; it may be because of the different atomic mass, energy, and diameter of deposition ions/atoms as well as the different mechanisms of film growth. The effect of other factors contributing to stress distribution at these interfaces will be studied in our future work.

**Acknowledgments** The authors in this work are supported by the General Administration of Quality Supervision, Inspection and Quarantine (AQSIQ) of P. R. China, with funding No. ALC1306 and the National Science Foundation of China (No. 51522106). Samples for film preparation and helpful discussion from Dr. P. Guo are also appreciated.

- 1) B. W. Sheldon, K. H. A. Lau, and A. Rajamani, *J. Appl. Phys.* **90**, 5097 (2001).
- 2) C. Yang and J. Pham, *Silicon* **7**, 27 (2015).
- 3) S. L. Chen, B. Shen, J. G. Zhang, L. Wang, and F. H. Sun, *Trans. Nonferrous Met. Soc. China* **22**, 3021 (2012).
- 4) Z. Nibennanoune, D. George, F. Antoni, S. Ahzia, D. Ruch, J. Gracio, and Y. Remond, *Diamond Relat. Mater.* **22**, 105 (2012).
- 5) X. J. Zheng, J. Y. Li, and Y. C. Zhou, *Acta Mater.* **52**, 3313 (2004).
- 6) C. H. Ma, J. H. Huang, and H. Chen, *Thin Solid Films* **418**, 73 (2002).
- 7) A. J. Wilkinson, D. J. Dingley, and G. Meaden, *Electron Backscattering Diffraction in Materials Science* (Springer, New York, 2009) 2nd ed., p. 231.
- 8) H. F. Poulsen, J. A. Wert, J. Neuefeind, V. Honkimäki, and M. Daymond, *Nat. Mater.* **4**, 33 (2005).
- 9) M. Ojima, Y. Adachi, S. Suzuki, and Y. Tomota, *Acta Mater.* **59**, 4177 (2011).
- 10) A. J. Wilkinson and T. B. Britton, *Mater. Today* **15**, 366 (2012).
- 11) V. Tong, J. Jiang, A. J. Wilkinson, and T. B. Britton, *Ultramicroscopy* **155**, 62 (2015).
- 12) T. B. Britton, J. Jiang, R. Clough, E. Tarleton, A. I. Kirkland, and A. J. Wilkinson, *Ultramicroscopy* **135**, 126 (2013).
- 13) A. J. Wilkinson, G. Meaden, and D. J. Dingley, *Mater. Sci. Technol.* **22**, 1271 (2006).
- 14) A. J. Wilkinson, G. Meaden, and D. J. Dingley, *Ultramicroscopy* **106**, 307 (2006).
- 15) X. Li, Z. Li, X. F. Tao, L. L. Ren, S. T. Gao, and G. F. Xu, *Mater. Lett.* **132**, 285 (2014).
- 16) X. Li, Z. Li, L. L. Ren, S. T. Gao, G. F. Xu, and X. F. Tao, *Mater. Lett.* **137**, 389 (2014).
- 17) A. J. Wilkinson, *Ultramicroscopy* **62**, 237 (1996).
- 18) A. M. Fincham and G. R. Spedding, *Exp. Fluids* **23**, 449 (1997).
- 19) S. Zhang, H. T. Johnson, G. J. Wagner, W. K. Liu, and K. J. Hsia, *Acta Mater.* **51**, 5211 (2003).
- 20) M. W. Thompson, *Phys. Rep.* **69**, 335 (1981).
- 21) Y. Lifshitz, *Diamond Relat. Mater.* **8**, 1659 (1999).
- 22) S. Uhlmann, T. Frauenheim, and Y. Lifshitz, *Phys. Rev. Lett.* **81**, 641 (1998).
- 23) N. Kaiser, *Appl. Opt.* **41**, 3053 (2002).
- 24) W. D. Nix and B. M. Clemens, *J. Mater. Res.* **14**, 3467 (1999).
- 25) L. B. Freund and E. Chason, *J. Appl. Phys.* **89**, 4866 (2001).
- 26) J. A. Floro, E. Chason, R. C. Cammarata, and D. J. Srolovitz, *MRS Bull.* **27** [01], 19 (2002).
- 27) H. Z. Yu and C. V. Thompson, *Acta Mater.* **67**, 189 (2014).